Supplementary Material

SM1 Fans location and geometry

Location and geometry of the 69 fans we used for morphometric analysis in this study.

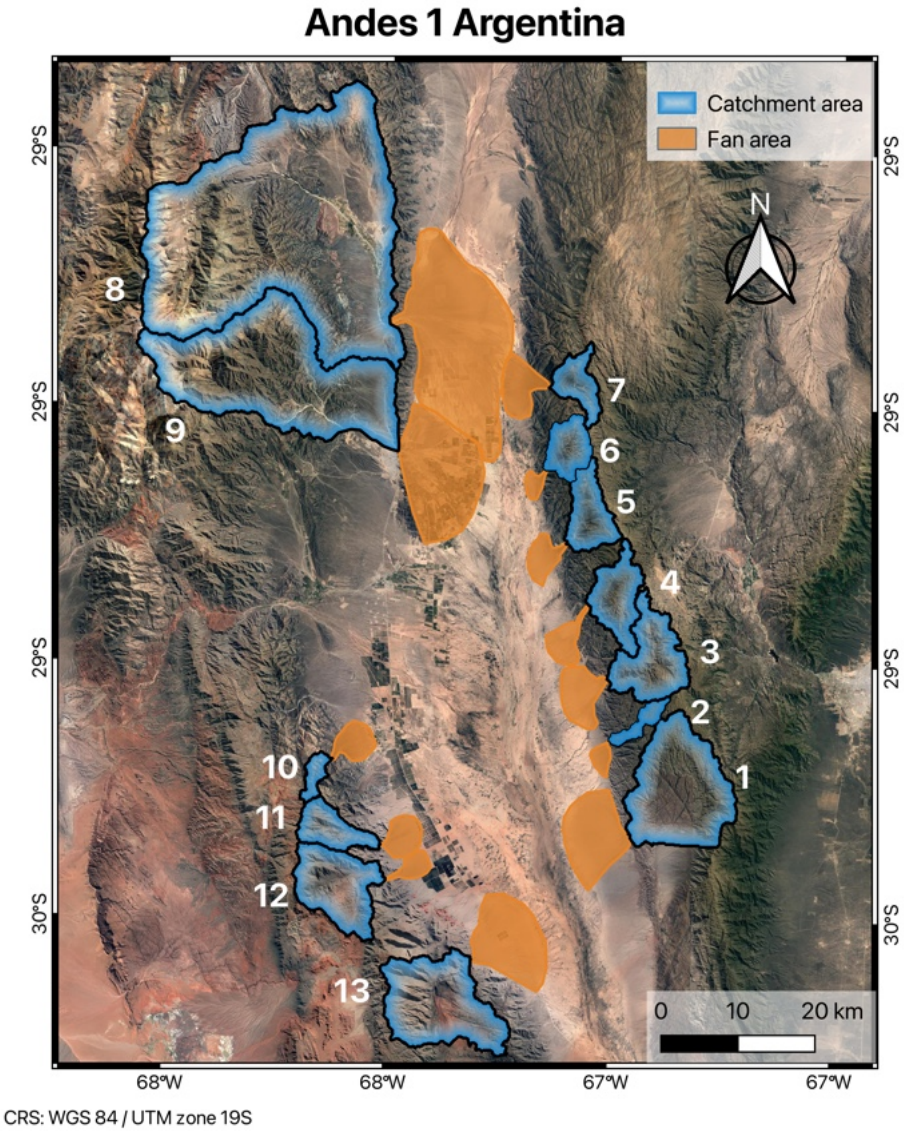

Figure S1: Location of fans(orange filled areas) and upstream feeding areas (blue and white lines) in Argentinian Andes (location 1).

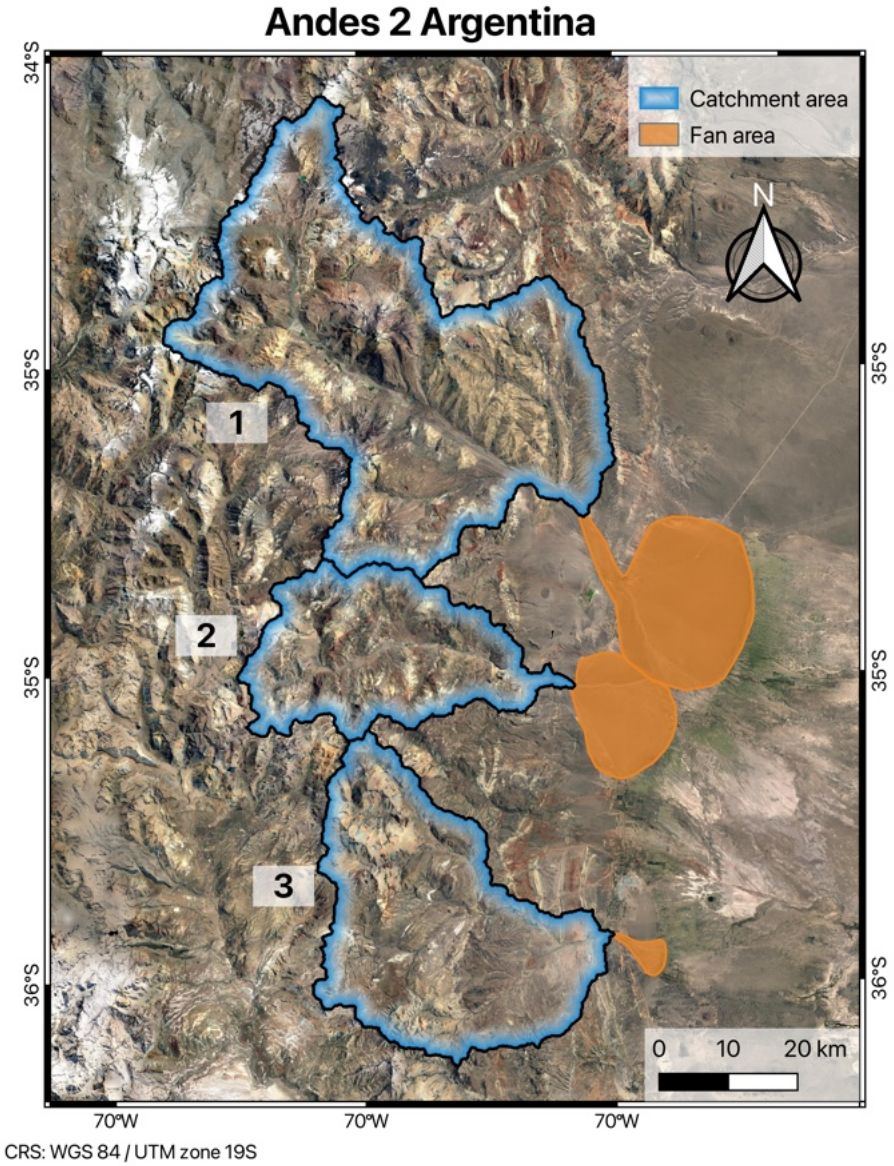

Figure S2: Location of fans(orange filled areas) and upstream feeding areas (blue and white lines) in Argentinian Andes (location 2).

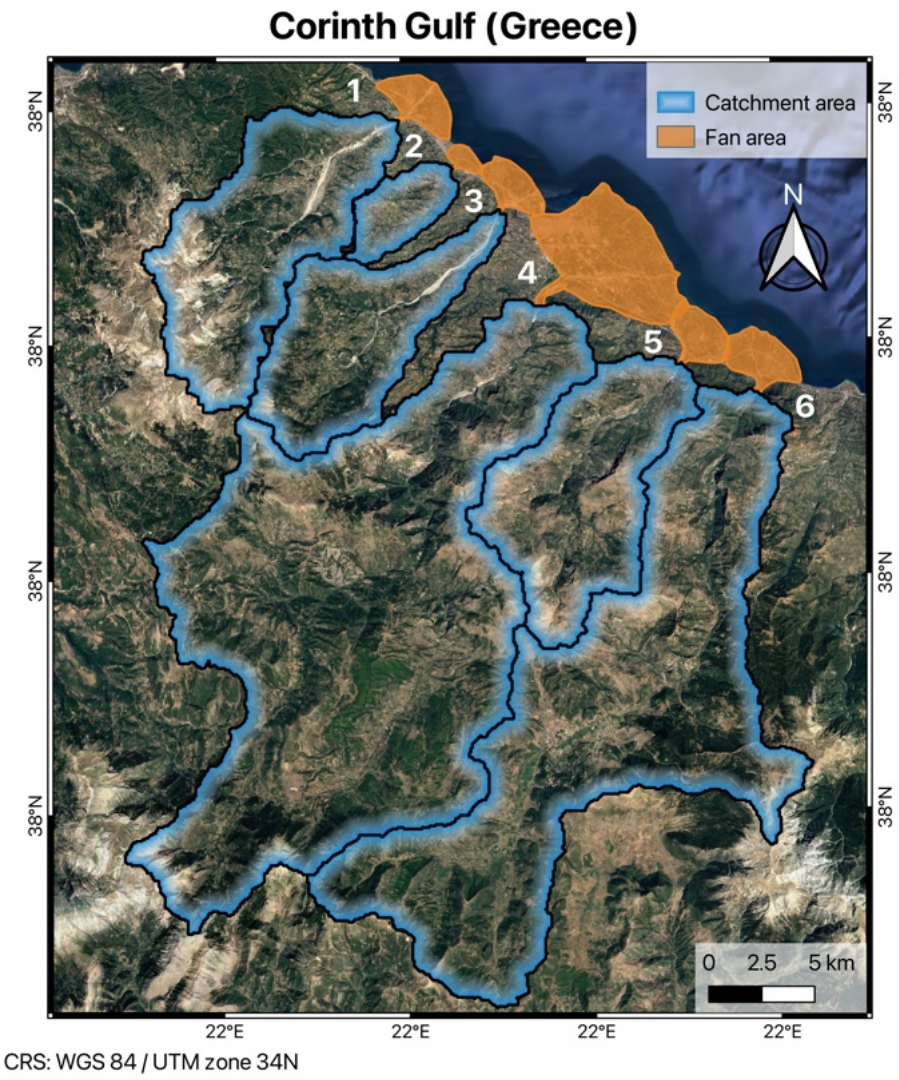

Figure S3: Location of fans(orange filled areas) and upstream feeding areas (blue and white lines) in the Gulf of Corinth, Greece.

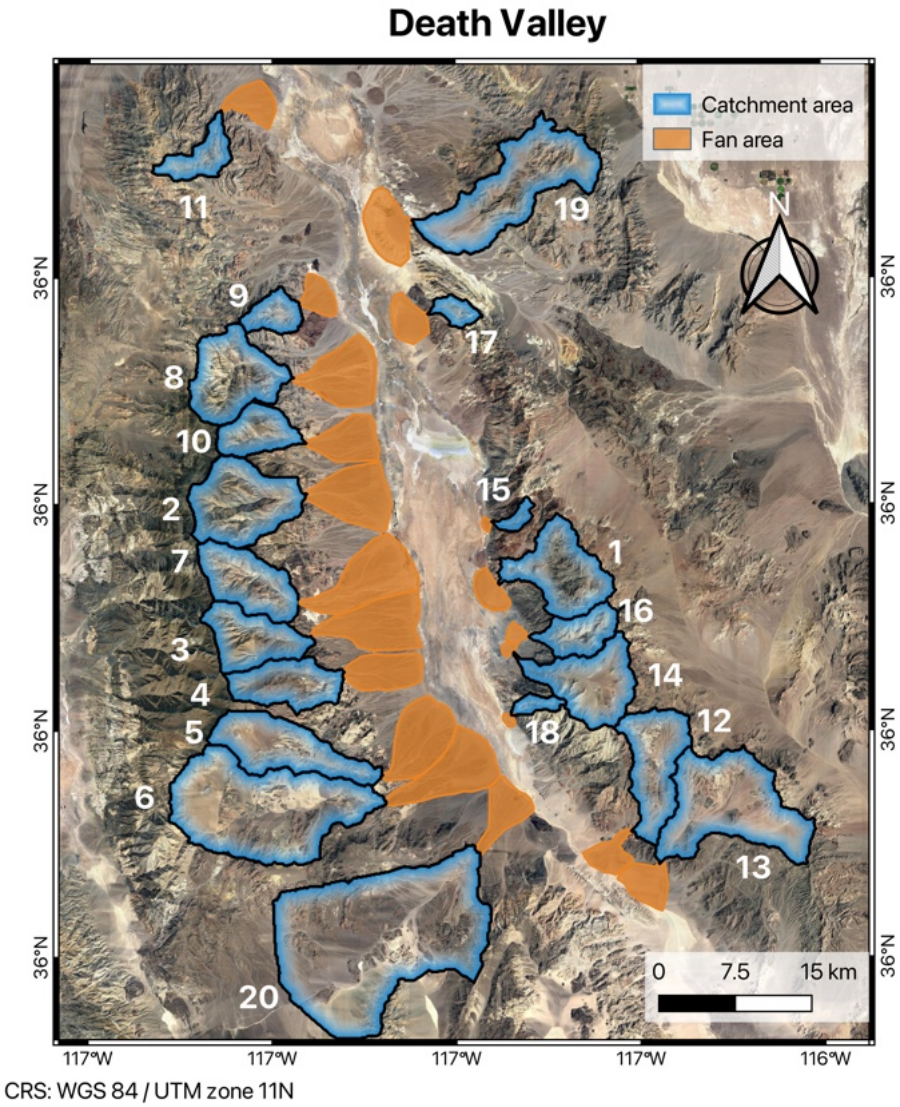

Figure S4: Location of fans(orange filled areas) and upstream feeding areas (blue and white lines) in Death Valley, California.

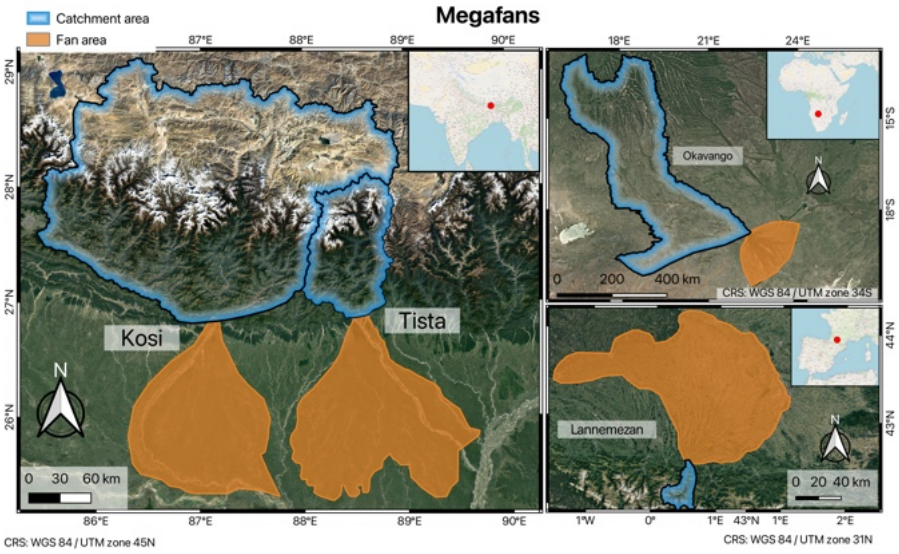

Figure S5: Location of fans(orange filled areas) and upstream feeding areas (blue and white lines) for three mega-fans, two along the Himalayan front (left panel), one in Botswana (top right panel) and one in southwestern France (bottom right panel).

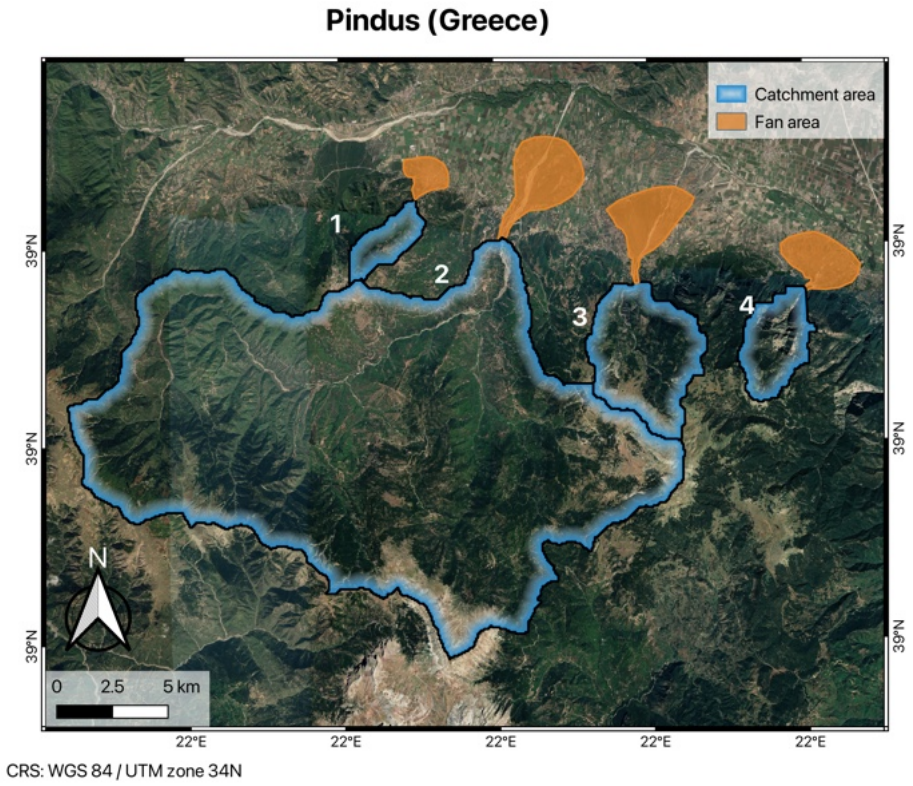

Figure S6: Location of fans(orange filled areas) and upstream feeding areas (blue and white lines) in the Pindus area (Greece).

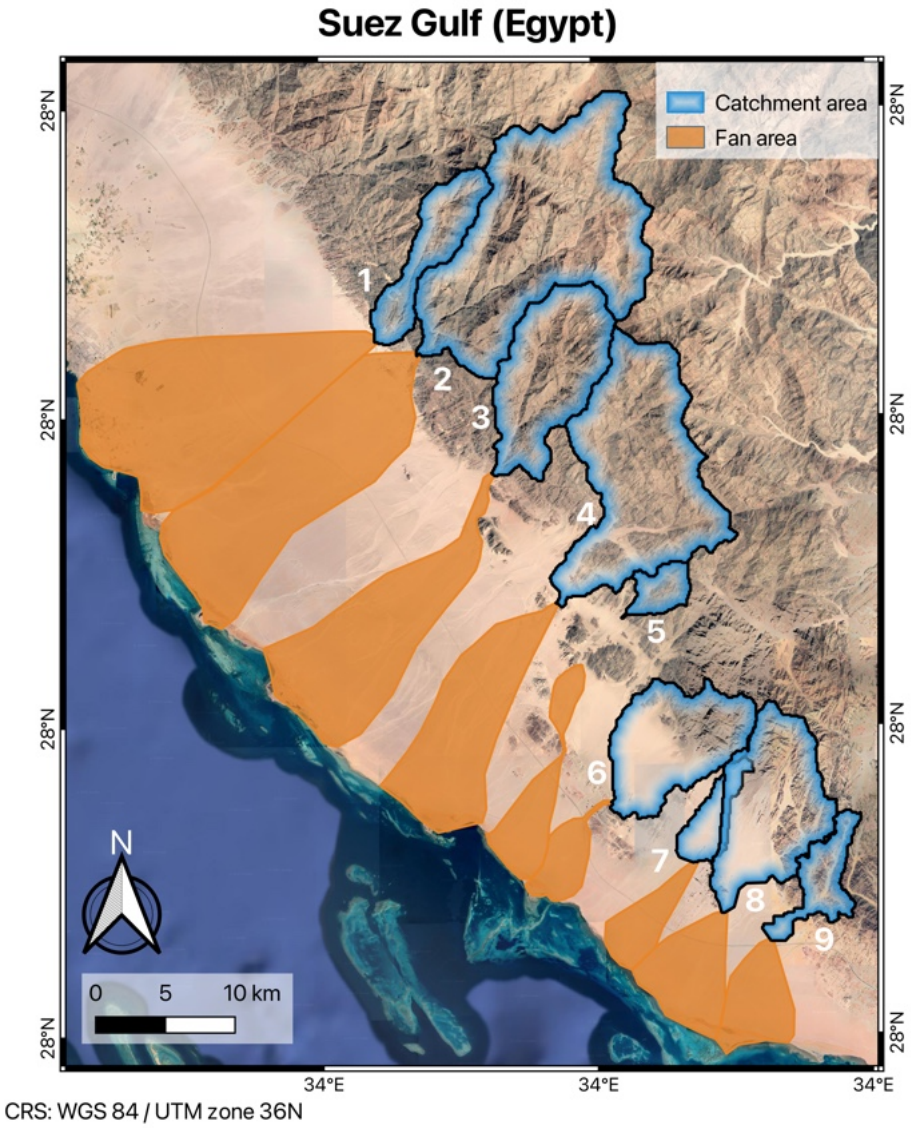

Figure S7: Location of fans(orange filled areas) and upstream feeding areas (blue and white lines) Along the Gulf of Suez in Egypt.

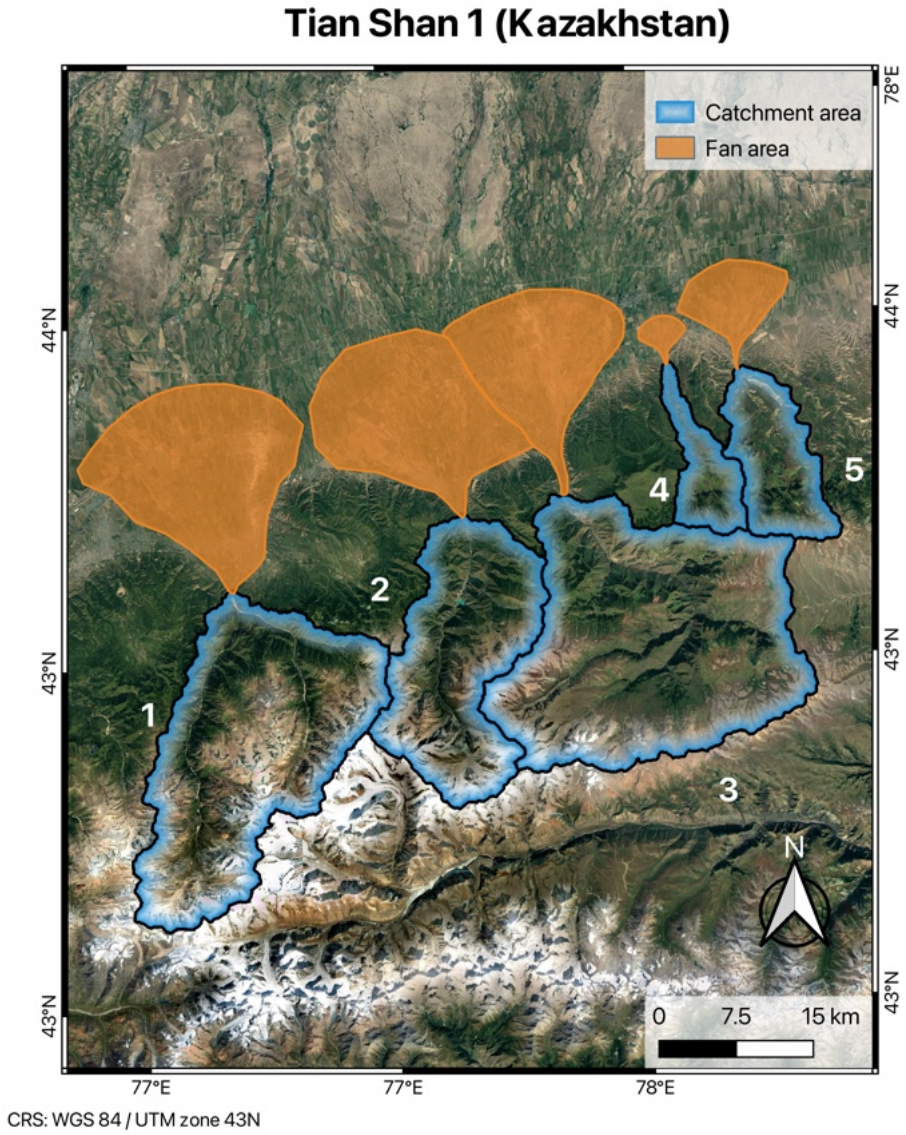

Figure S8: Location of fans(orange filled areas) and upstream feeding areas (blue and white lines) in the Tian Chan in Kazakhstan.

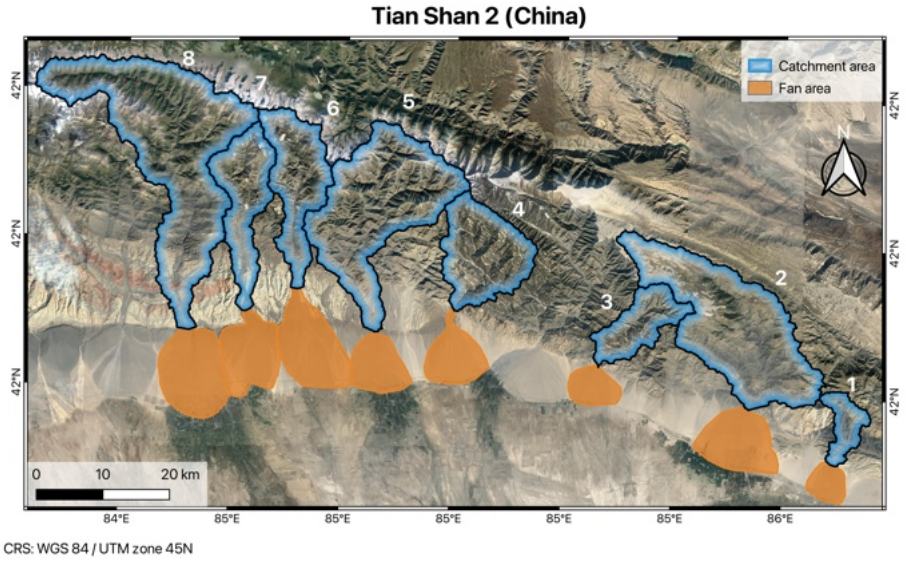

Figure S9: Location of fans(orange filled areas) and upstream feeding areas (blue and white lines) in the Tian Chan in China.

SM2 Fan size versus upstream source area size relationship including megafans

In Figure S10, we show plots similar to those shown in Figure 2 but in which we have included data from four large or so-called "megafans", namely the Okavango, Lannemezan, Kosi and Tista megafans.

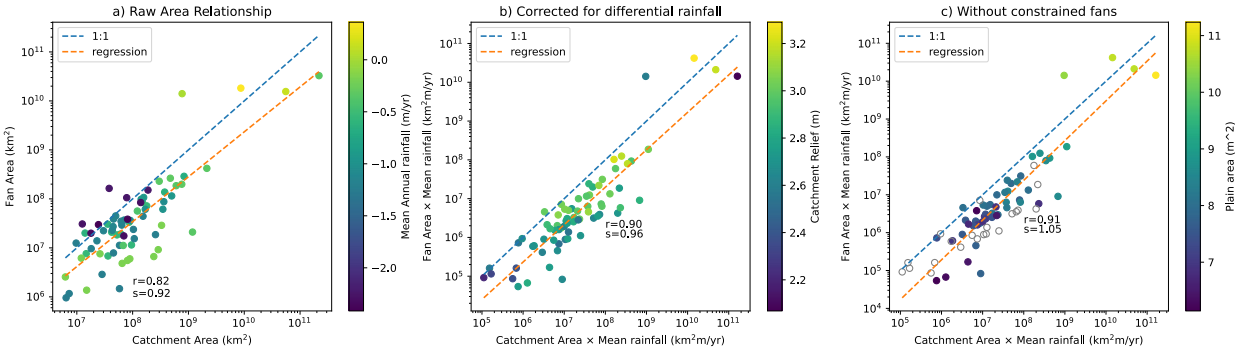

Figure S10: a) Fan area vs source area relationship from 70 fan worldwide, excluding megafans. b) Corrected for differential rainfall between source and fan areas. c) After removing constrained fan data.

We see that the addition of these very large fans strongly influence the relationship between fan extend and upstream source area size in such a way that it artificially biases the correlation coefficient and slope towards unity. However, despite this, the correlation is still marginally improved when the fan and upstream area sizes are weighted by their relative precipitation rate and when the constrained fans are removed from the regression.

SM3 Form and behavior of the analytical solution for fan geometry

We propose here a simple explanation of the form and behavior of the analytical solution for the surface topography of the sedimentary system given in Equation 2 that is constructed on the hypergeomotric function ${}_2F_1$. Two solutions are shown in Figure S11. The first (left column in Figure S11) corresponds to the situation where the size of the source area, A_0, is much smaller than the space available for the development of a fan, i.e., between the outlet of the source area to the base level (distance L). When weighed for a potential difference in rainfall between the source area, ν_0, and the sedimentary system, ν_f, the exact expression for this condition is that:

$$A_0 \ll (L/k)^{1/p} \nu_f / \nu_0 \tag{14}$$

We see that in that situation (Figure S11A), the solution is made of two parts, a steep, relatively linear part (thick line in each panel of Figure S11) corresponding to the fan and a more curved part characterized by gentler slopes that connects the fan to the base level (thin line in each panel of Figure S11) and corresponds to what we term the alluvial plain. We see that the transition between the two parts corresponds to the point of maximum curvature (Figure S11C).

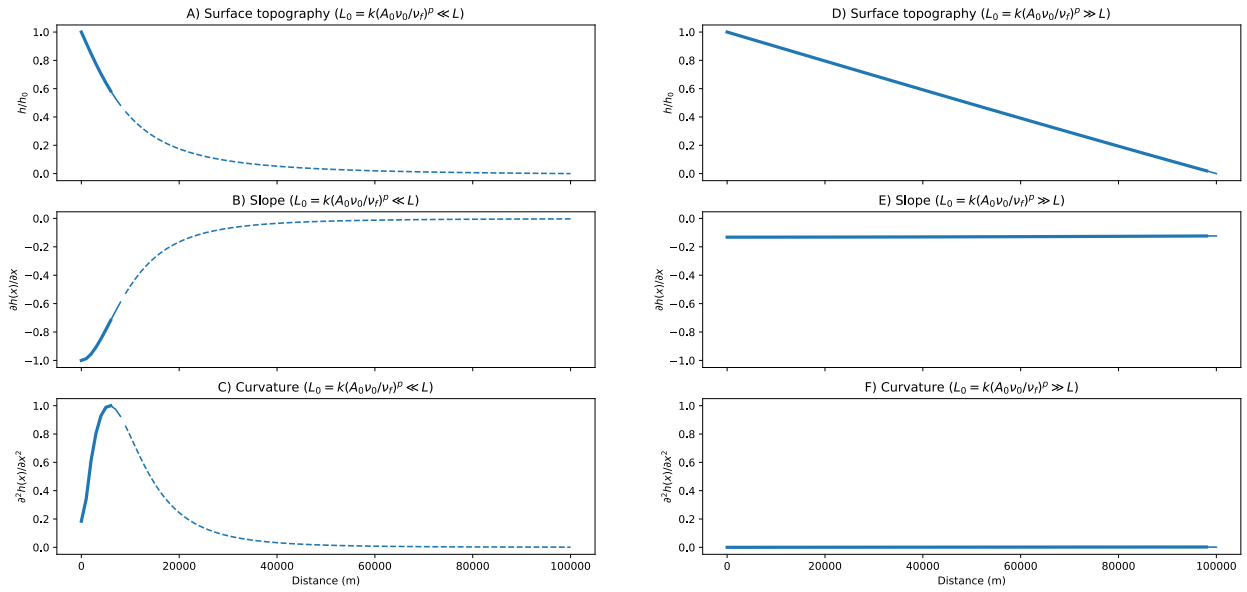

Figure S11: A) and D) Surface topography, H, B) and E) slope, $\partial h/\partial x$, and C) and F) curvature, $\partial^2 h/\partial x^2$ for two end-member cases. Left column (A to C) corresponds to a case with a small source area; right column (D to F) to a case with a very large source area.

The second case corresponds to situations where the size of the source area is much greater than the

space available for the fan to develop (right column in Figure S11). In this case, the solution corresponds to a straight, i.e., constant slope, surface from the fan apex to the base level (Figure S11A). The slope is constant (Figure S11) and the curvature is nil (Figure S11C).

In Figure S12, we show how the solution behaves as a function of its parameters, namely the ratio $(m+1)/n$, p, A_0 and ν_0. We see, for this intermediary case (i.e., where $A_0 \lesssim (L/k)^{1/p}\nu_f/\nu_0$) that the solution is only mildly sensitive to the exponent ratio, $(m+1)/n$, or Hack's Law exponent, p. But it is very and equally sensitive to the assumed upstream drainage area, A_0, or rainfall in the source area, ν_0, relative to the rainfall in the fan, ν_f.

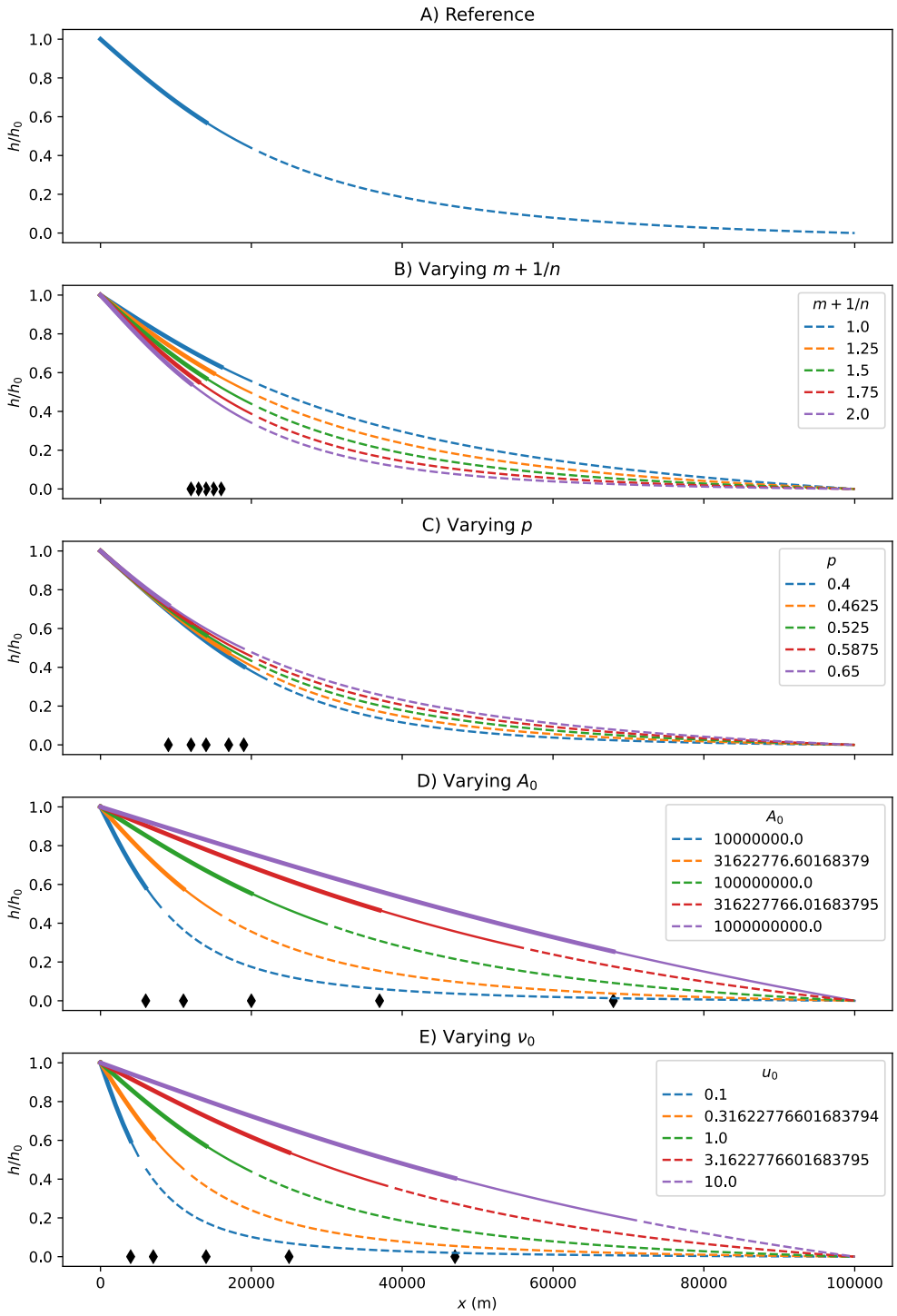

Figure S12: Sensitivity of the analytical solution to its parameters. A) Reference solution; B) solutions obtained by varying the ratio $(m+1)/n$ within the observed range [1-2]; C) solutions obtained by varying Hack's Law exponent, p within its observed range [0.4,0.65]; note that because k, the other Hack's Law parameter, has units that vary with p, it needs to co-vary with p for a realistic comparison; here we modified k according to $k' = kA_0^{(p-p')}$; D) solutions obtained varying A_0 by two orders of magnitude; and E) solutions obtained by varying ν_0 by two orders of magnitude.

SM4 Comparing theoretical shape to observed fan profiles

In Figure S13 to S15, we show the comparison between observed fan profiles extracted from SRTM data from 69 fans representing a wide range of environments where fans are formed with the analytical solution given in Equation 2. All parameters in Equation 2 are given commonly agreed values except for Hack's Law parameters, k and p, in Figure S13, the exponent ration, $(m+1)/n$ in Figure S14, and the upstream source area size, A_0, in Figure S15. The value of these parameters is obtained in each case by minimisation of the difference between the observed and theoretical profiles using a simplex method [43].

Figure S13: Topographic profiles across 69 fans compared to the analytical solution given by Equation 2. In each case, the best fit profile was obtained by finding the optimum value of the Hack's Law parameters, p and k, in Equation 2. Commonly accepted value for $(m+1)/n = 1.5$ was used. All other parameter values (h_0, A_0, L, ν_0 and ν_f) were derived from observational constraints.

Figure S14: Topographic profiles across 69 fans compared to the analytical solution given by Equation 2. In each case, the best fit profile was obtained by finding the optimum value of the ratio of exponents $(m+1)/n$, in Equation 2. Commonly accepted value for k and $p = 0.58$ were used. All other parameter values (h_0, A_0, L, ν_0 and ν_f) were derived from observational constraints.

Figure S15: Topographic profiles across 69 fans compared to the analytical solution given by Equation 2. In each case, the best fit profile was obtained by finding the optimum value of the upstream drainage area, A_0, in Equation 2. Commonly accepted value for k and $p = 0.58$ and $(m+1)/n = 1.5$ were used. All other parameter values (h_0, L, ν_0 and ν_f) were derived from observational constraints.

SM5 Range of fan geometries that can be derived from the analytical solution, depending on the ratio A_0/kL^p.

In Figure S16, we show a series of profiles derived from Equation 2 where we varied the value of the upstream source catchment area, A_0. We see that when $A_0^* = \frac{A_0}{(L/k)^{1/p}} \frac{\nu_0}{\nu_f} << 1$, the theoretical profile is made of two parts: a relatively linear segment and a curved section. The dot corresponds to the transition between the linear segment that corresponds to the fan, and the curve section that corresponds to the alluvial plain, is located at a distance $x/L = A0^*$ from the fan apex. For values of $A_0^* \geq 1$, the profile is almost perfectly linear and the curve section is missing. The analytical expression that we propose (Equation 2) can therefore differentiate between two commonly observed types of fans [1]: those that connect to an alluvial plain and those that are "constrained" in their extent by the proximity of the fan apex to the base level.

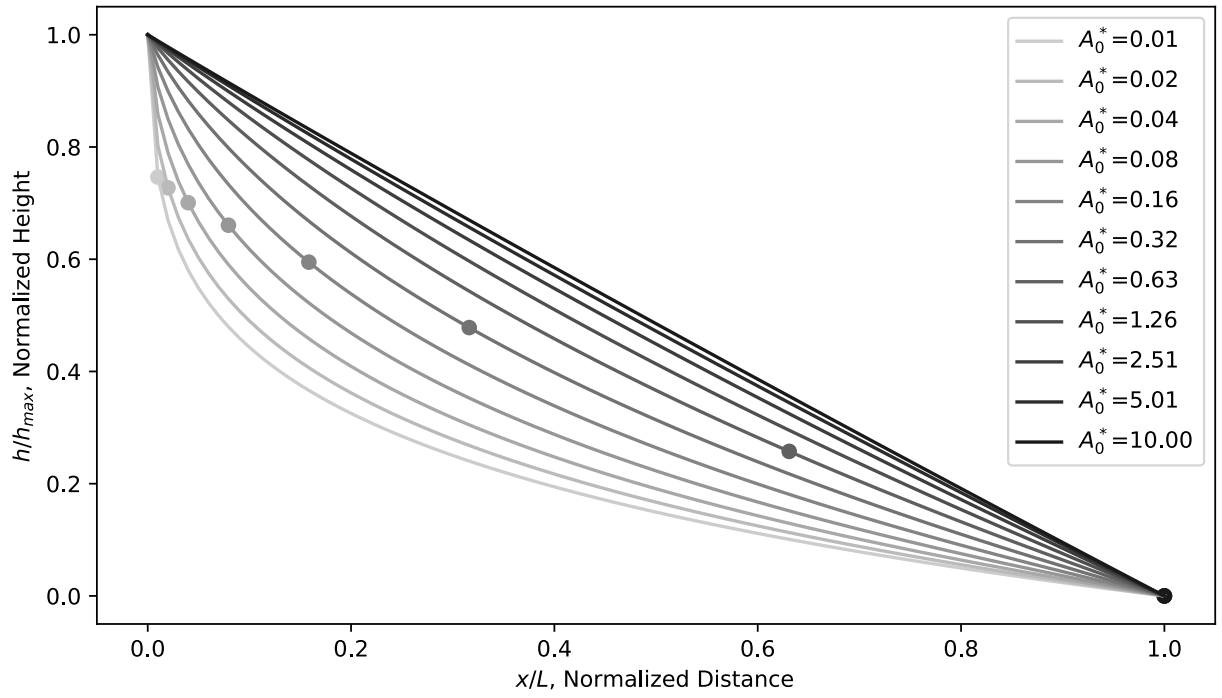

Figure S16: Range of profiles that can be obtained by varying the contribution to discharge from the source area, i.e., $A_0^* = \frac{A_0}{(L/k)^{1/p}} \frac{\nu_0}{\nu_f} << 1$. For each curve, the circle corresponds to the location of the transition from fan to alluvial plain.

SM6 Fan slope vs fan upstream source area relationship

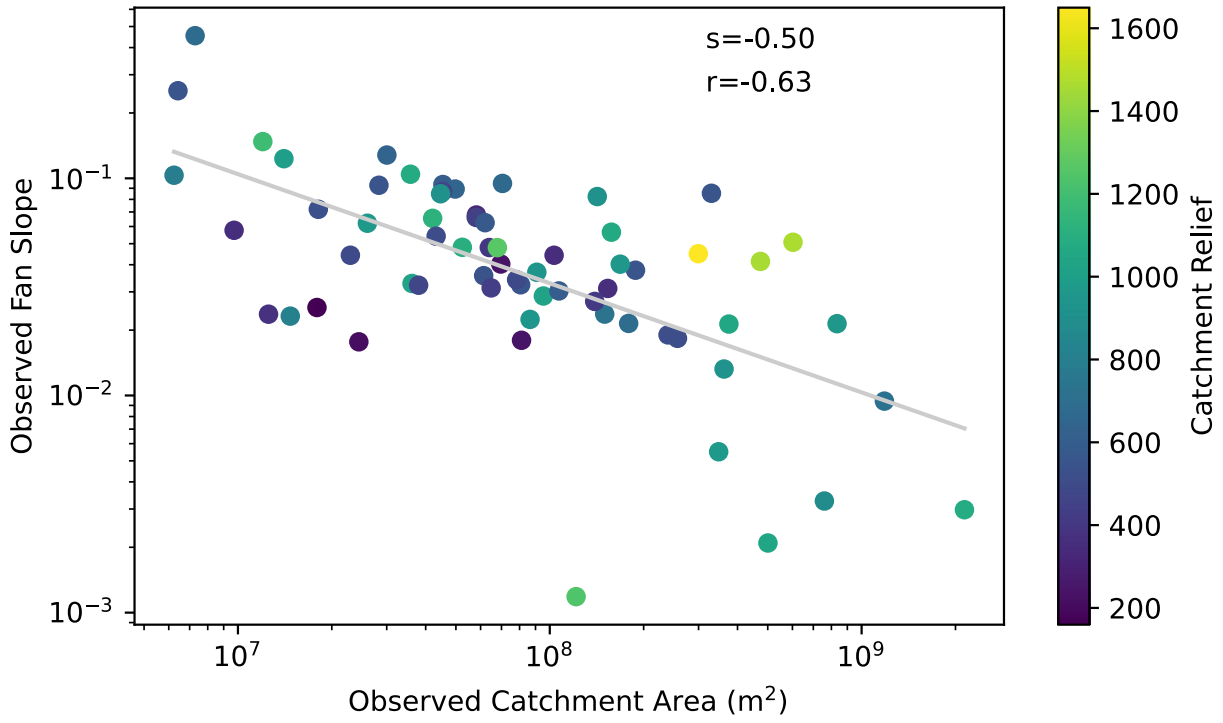

Figure S17: a) Observed relationship between fan slope (near the apex) and upstream source catchment area, coloured by catchment relief. b) Same relationship but applied to the slope and area derived from the best-fit theoretical profile obtained by optimisation. Note that, to avoid bias resulting from their large size, the regression was computed by excluding the four megafans.

SM7 Two-dimensional numerical solutions

We used a two-dimensional landscape evolution model to reproduce the analytical solution given in Equation 2 and to compute the effect of basement subsidence on the fan geometry. The model solves the following evolution equation for the topographic height, h:

$$\frac{\partial h}{\partial t} = U - K_f q_w^m S^n + G\frac{q}{q_w} \tag{15}$$

where U is uplift or subsidence rate, K_f is the erodibility, q_w is discharge, S is topographic slope, G is a dimensionless deposition coefficient and q is sediment flux obtained by integrating upstream erosion/deposition. We used standard values for the various coefficient, i.e., $K_f = 1 \times 10^{-5}$ m$^2 - m$/yr, $m = 0.45$, $n = 1$ and $G = 1$. We solved the equation in a square area of size 100×100 km^2 that represents a half fan. Sediment and discharge from a hypothetical source area are provided in the bottom left corner. The bottom and left boundaries are reflective (no flux) boundaries, while to the top and right boundaries are set at base level($h = 0$). The uplift rate, U_0 and precipitation rate in the bottom left corner are set to mimic a source area of size A_0 providing a sediment flux equal to $A_0 \times U_0$. Subsidence in the rest of the model follows an exponential decrease from the bottom corner according to the following equation:

$$U_0 = -\dot{s} = -\dot{s}_0 \mathbf{e}^{-r/\alpha} \tag{16}$$

where r is the radial distance to the bottom left corner which will become the fan apex. The equation is solved for 10 Myr, to ensure that the system reaches mean topographic steady-state. This means that the topography averaged over many time steps reaches a steady-state form but that the topography varies dynamically in response to avulsion of the main channel.

We first demonstrate in Figure S18 that the numerical model reproduces the analytical solution given in Equation 2. For this we performed three numerical simulation varying the size of the upstream area, A_0, while setting the subsidence to zero. We see that the numerical fan topography shown as a set of profiles in the left panels of Figure S18 are almost identical to the theoretical solution. The grey lines correspond to individual profiles sampled across the middle of the model at 50 different times once the model has reached steady-state. The black line with crosses represent the mean of these grey curves. The red line is the analytical solution. The central panels show the corresponding predicted topography in plan-form. The right panels of Figure S18 show the distribution of discharge which can be regarded as a plan view of active channels. We see that, despite the divergent shape of the fan topography, the channels form a network that results in an increase of drainage area and thus discharge with distance

from the fan apex. The best fit to the analytical solution is obtained for a Hack exponent of $p = 2$ in the analytical solution.

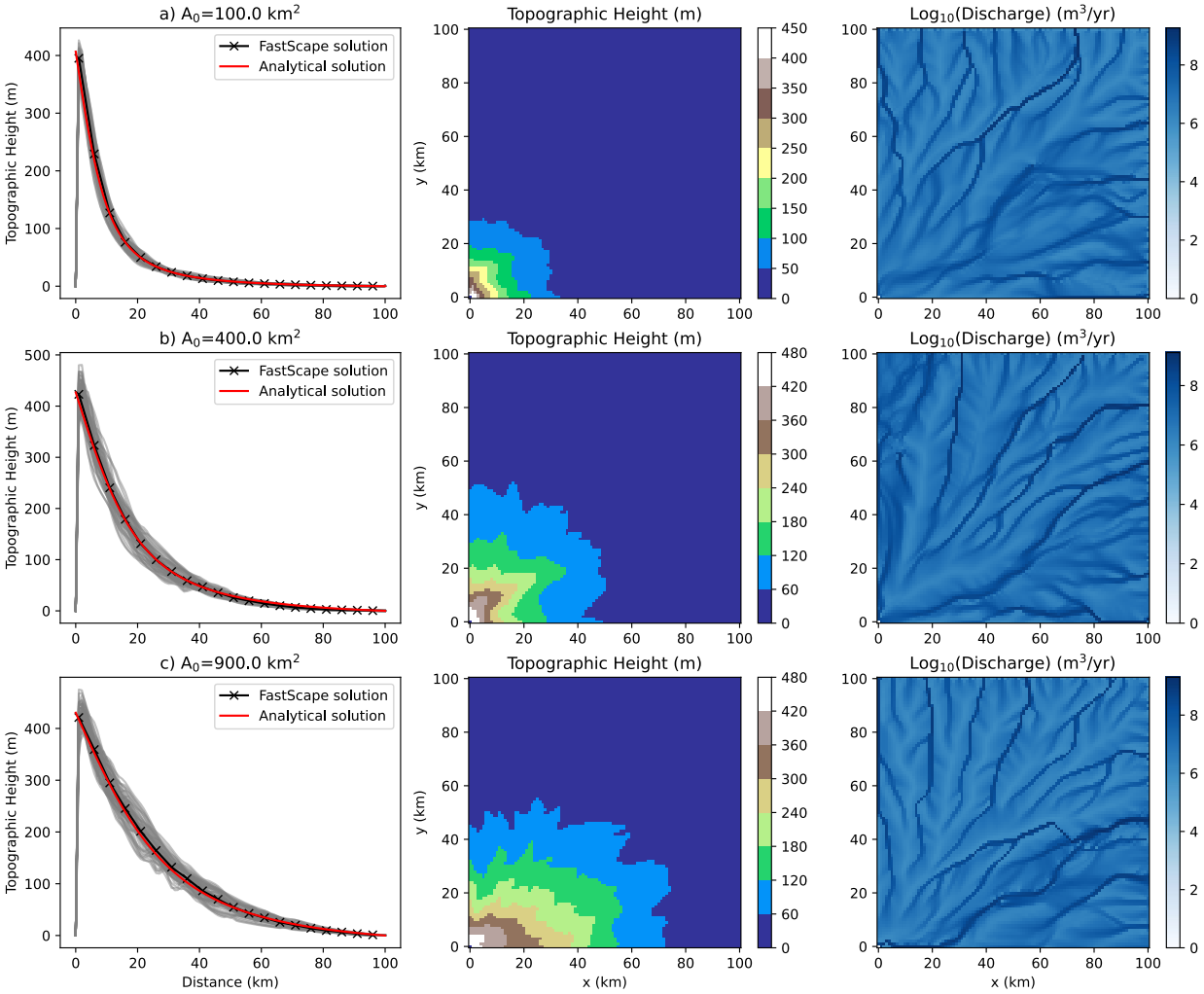

Figure S18: Comparison between numerical model predictions and analytical solution for three values of the upstream source area, A_0. Left panels show topographic profile across the diagonal of the model from the fan apex in the bottom left corner. Middle panels show predicted surface topography at the end of the simulation and left panels show computed discharge.

Note that a recent study [47] has also reproduced the observed relationship between fan area and upstream catchment area but also reported a strong sensitivity of fan area to other forcings and model parameters, including uplift rate in the source area and thus sediment flux, transport length, and mean precipitation rate. No simple explanation is provided for this model behaviour.

We then performed a series of 121 numerical experiments in which we varied the maximum subsidence

rate, $\dot{s}_0$, and its extent, α while keeping all other parameters constant, including A_0 that we fixed at 20 km^2. In each experiment, the subsidence rate is set according to a prescribed value of the parameter F that is defined as the ratio of the flux being deposited in the basin to the incoming flux form the source area. If $F = 1$, all sediment entering the system from the source area is deposited in the basin and none leaves the modeled domain; for large values of F compared to unity, the basin tends towards bypass as none of the sediments coming from the source area are deposited in the basin. We chose 11 values of α between 5 and 50 km that span across a range centered on the source area linear size, 20 km, but do not exceed the half size of the integration domain, $L = 100$ km. We also chose 11 values for F in the range $[1.25 - 10]$ from which the corresponding value of the maximum subsidence rate, $\dot{s}_0$ can be computed according to:

$$\dot{s}_0 = \frac{2U_0A_0}{F\pi\alpha^2} \tag{17}$$

The results of these 121 experiments are shown in Figure S19 as plots of the topographic profile across the diagonal of the fan (black line) and its comparison to the analytical solution (red line). The grey lines correspond to topographic profiles at various time steps in the models evolution. We see that it is only for experiments characterized by a small value of α compared to the source area linear dimension (20 km) or for values of F close to unity (all the sediment is deposited in the basin) that the numerical solution differs from the analytical solution. Interestingly, in these cases, the size of the fan is larger than the theoretical solution that assumes no subsidence, whereas the extent of the subsidence is smaller than the theoretical size of the fan. This shows that the fan extent is only marginaly related to the extent of the subsidence function.

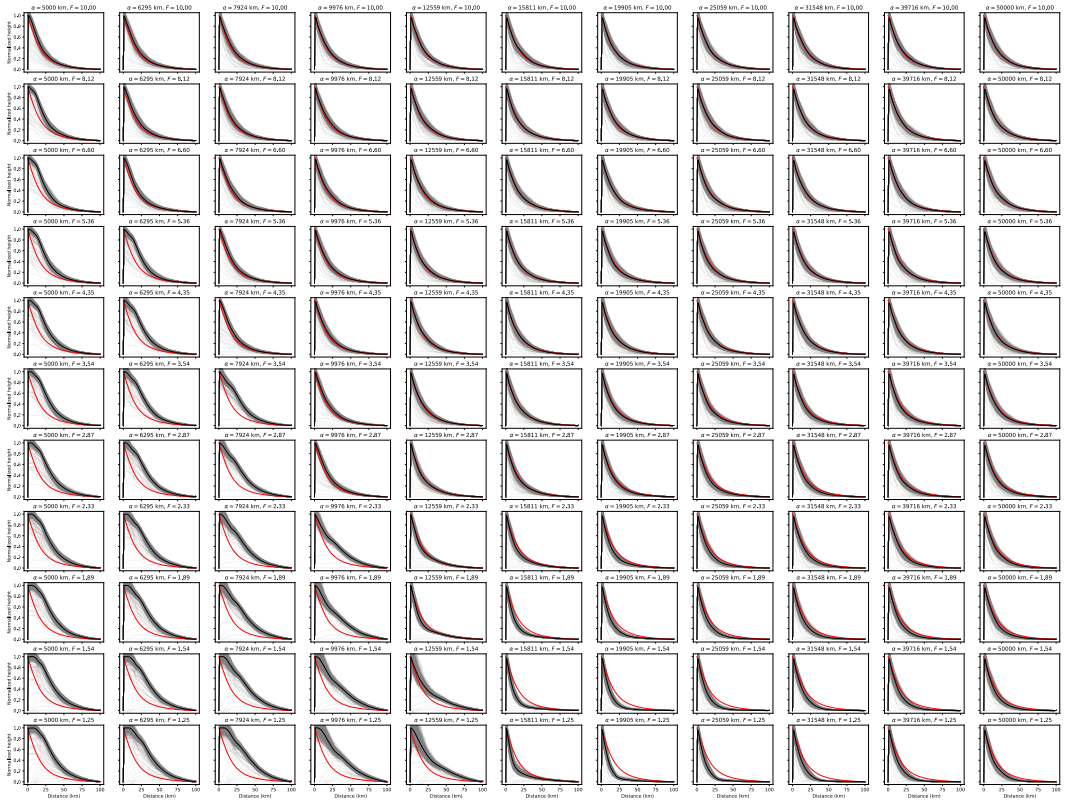

Figure S19: Importance of subsidence on fan geometry for various values of the subsidence rate F and extent α. In each panel are shown the theoretical 1D profile without subsidence from Equation 2 (red line), profile along middle of the fan obtained from 2D LEM (black line is time-average of grey lines).

SM8 Animation

Animation produced from the solution of Equation 15 where $U = 0$, $K_f = 1 \times 10^{-5}$ m^{2-m}/yr, $m = 0.45$, $n = 1$, $G = 1$ and $A_0 = 400$ m^2. The flux q_0 and discharge coming from the upstream catchment of size A_0 are imposed at one node $(x = 0, y = 0)$ and are scaled to produce a fan that is approximately 80 m high at its apex. The domain is 4 by 2 km in length and discretized by 401 by 201 nodes. The solution is computed over 2 Myr with 2000 time steps. All steps are used to produce the animation. For each frame, the deposition rate is contoured using green colors for negative values (net erosion) and red colors for positive values (net deposition). Note the asymmetry in the color map such that areas in yellow experience no net erosion or deposition. Parts of the solution where drainage area is above a given threshold are shown in blue and represent the position of the active channels.

During the first half of the model evolution ($t < 500$ kyr), the system is in an aggradation phase that leads to the building of the fan structure. It reaches a quasi-steady-state form at approximately $t = 500$ kyr. From that point onward, deposition (red areas) takes place around the main channel, i.e., the channel fed by the upstream catchment and erosion (green areas) takes place around all the other channels, i.e., those that are not connected to the upstream catchment. Frequent large-scale avulsions take place that originate at or near the fan apex. These leads to a rapid shift of the main depositional domain towards the base of the fan followed by a long period of aggradation from base to apex along the main channel. This dynamics is very similar to that observed (or inferred) for many active fans. See, for example, Figure S20 [1].

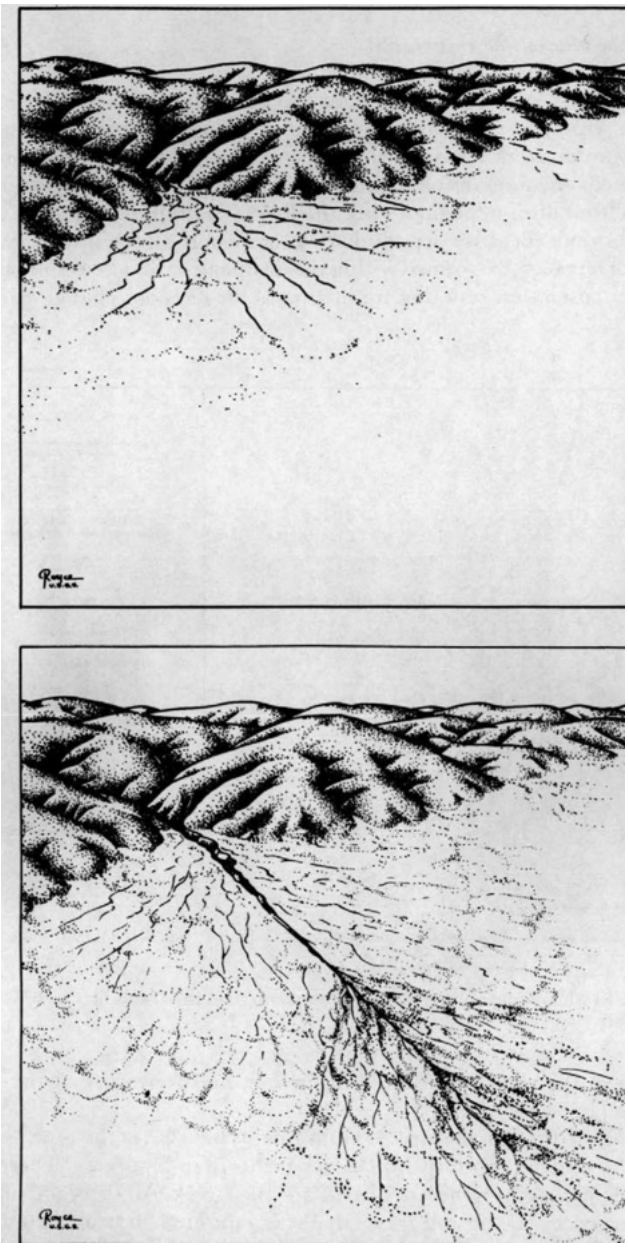

Figure S20: Development of a segmented alluvial fan where the area of deposition has shifted downslope from the mountain front [1]. **a** Unentrenched alluvial fan before period of accelerated stream-channel downcutting. **b** Entrenched alluvial fan, where the area of deposition has shifted down fan.

SM9 Mathematical derivation of the analytical solution for the surface topography

In a sedimentary system experiencing negligible subsidence, the flux of material at any point, x, through the system must be equal to the flux of material leaving the source area, q_0. Assuming that sedimentary flux is proportional to the product of discharge, Q, (to the power $m+1$) and slope, S, (to the power n), we can write:

$$q_0 = K_d\Big(\frac{Q}{w}\Big)^{m+1}|S|^n \tag{18}$$

where K_d is a transport coefficient, and w the width of the main channel connecting the source area to the base of the sedimentary system.

We further assume that discharge along the main channel is the sum of what arrives at the apex of the sedimentary system from the source area, i.e., $A_0\nu_0$, plus the contribution of what rains and accumulates on the fan:

$$Q = A\nu = A_0\nu_0 + (\frac{x}{k})^{1/p}\nu_f \tag{19}$$

where A_0 is the drainage area of the source area and ν_0 and ν_f are the rainfall in the source area and sedimentary system, respectively. k and p are Hack's Law parameters.

Slope is equal to the spatial derivative of surface topography, h. We can thus write:

$$S = \frac{\partial h}{\partial x} = -\Big(\frac{q_0 w^{m+1}}{K_d(A_0\nu_0)^{m+1}(1+(\frac{x}{k})^{1/p}\frac{\nu_f}{A_0\nu_0})^{m+1}}\Big)^{1/n} \tag{20}$$

Introducing a dimensionless distance x':

$$x' = \frac{x}{k}(\frac{\nu_f}{A_0\nu_0})^p \tag{21}$$

and noting that:

$$\frac{\partial h}{\partial x'} = \frac{\partial h}{\partial x}|_{x=x'}\frac{\partial x}{\partial x'} \tag{22}$$

yields:

$$\frac{\partial h}{\partial x'} = -(\frac{q_0 w^{m+1}}{K_d(A_0\nu_0)^{m+1}})^{1/n}\frac{1}{(1+x'^{1/p})^{(m+1)/n}}k(\frac{A_0\nu_0}{\nu_f})^p \tag{23}$$

as:

$$x = kx'(\frac{A_0\nu_0}{\nu_f})^p \tag{24}$$

and thus:

$$\frac{\partial x}{\partial x'} = k(\frac{A_0\nu_0}{\nu_f})^p \tag{25}$$

Introducing $h' = h/h_0$ with

$$h_0 = (\frac{q_0 w^{m+1}}{K_d (A_0 \nu_0)^{m+1}})^{1/n} k (\frac{A_0 \nu_0}{\nu_f})^p \tag{26}$$

yields the dimensionless form of the equation governing the slope of the sedimentary system:

$$\frac{\partial h'}{\partial x'} = -(\frac{1}{1 + x'^{1/p}})^{\frac{m+1}{n}} \tag{27}$$

which has the following general solution:

$$h'(x') = -x' \ {}_2F_1(\frac{m+1}{n}, p; p+1; -x'^{1/p}) + C \tag{28}$$

The constant C can be derived from the boundary condition at $x = L$:

$$h(x = L) = h'(x' = \frac{L}{k}(\frac{\nu_f}{A_0 \nu_0})^p) = 0 \tag{29}$$

to yield:

$$C = L' \ {}_2F_1(\frac{m+1}{n}, p; p+1; -L'^{1/p}) \tag{30}$$

where:

$$L' = \frac{L}{k}(\frac{\nu_f}{A_0 \nu_0})^p \tag{31}$$

The solution takes the following form:

$$h(x) = (\frac{q_0 w^{m+1}}{K_d (A_0 \nu_0)^{m+1}})^{1/n} [\psi(L) - \psi(x)] \tag{32}$$

where:

$$\psi(x) = x \ {}_2F_1(\frac{m+1}{n}, p; p+1; -(\frac{x}{k})^{1/p} \frac{\nu_f}{A_0 \nu_0}) \tag{33}$$